Noncollinear ferromagnetic Weyl semimetal with anisotropic anomalous Hall effect

Hung-Yu Yang [1] Bahadur Singh,[2] Jonathan Gaudet,[3] Baozhu Lu [4] Cheng-Yi Huang,[5] Wei-Chi Chiu [5]
Shin-Ming Huang [6] Baokai Wang,[5] Faranak Bahrami,[1] Bochao Xu,[7] Jacob Franklin,[7] Ilya Sochnikov [7,8] David E. Graf,[9]
Guangyong Xu,[10] Yang Zhao [10] Christina M. Hoffman,[11] Hsin Lin [12] Darius H. Torchinsky,[4] Collin L. Broholm,[3]
Arun Bansil,[5,*] and Fazel Tafti [1,†]

[1]*Department of Physics, Boston College, Chestnut Hill, Massachusetts 02467, USA*
[2]*Department of Condensed Matter Physics and Materials Science, Tata Institute of Fundamental Research, Colaba, Mumbai 400005, India*
[3]*Institute for Quantum Matter and Department of Physics and Astronomy, The Johns Hopkins University, Baltimore, Maryland 21218, USA*
[4]*Department of Physics and Temple Materials Institute, Temple University, Philadelphia, Pennsylvania 19122, USA*
[5]*Department of Physics, Northeastern University, Boston, Massachusetts 02115, USA*
[6]*Department of Physics, National Sun Yat-sen University, Kaohsiung 80424, Taiwan*
[7]*Department of Physics, University of Connecticut, Storrs, Connecticut 06269, USA*
[8]*Institute of Material Science, University of Connecticut, Storrs, Connecticut 06269, USA*
[9]*National High Magnetic Field Laboratory, Tallahassee, Florida 32310, USA*
[10]*NIST Center for Neutron Research, National Institute of Standards and Technology, Gaithersburg, Maryland 20899-6102, USA*
[11]*Neutron Scattering Division, Oak Ridge National Laboratory, Oak Ridge, Tennessee 37831, USA*
[12]*Institute of Physics, Academia Sinica, Taipei 11529, Taiwan*

An emerging frontier in condensed matter physics involves novel electromagnetic responses, such as the anomalous Hall effect (AHE), in ferromagnetic Weyl semimetals (FM-WSMs). Candidate FM-WSMs have been limited to materials that preserve inversion symmetry and generate Weyl crossings by breaking the time-reversal symmetry. These materials share three common features: a centrosymmetric lattice, a collinear FM ordering, and a large AHE observed when the field is parallel to the magnetic easy axis. Here we present CeAlSi as a FM-WSM in which the Weyl nodes are stabilized by breaking the inversion symmetry, but their positions are tuned by breaking the time-reversal symmetry. Unlike the other FM-WSMs, CeAlSi has a noncentrosymmetric lattice, a noncollinear FM ordering, and a novel AHE that is anisotropic between the easy and hard magnetic axes. It also exhibits large FM domains that are promising for exploring both device applications and the interplay between the Weyl nodes and FM domain walls.

I. INTRODUCTION

Weyl nodes are protected linear crossings of two nondegenerate bands that lead to chiral relativistic quasiparticles [1,2]. In Weyl semimetals (WSMs), the presence of Weyl nodes at the Fermi level enables Berry phase engineering in the bulk, creates Fermi arcs on the surface, and leads to a host of emergent electromagnetic responses such as the topological Hall effect (THE) and the anomalous Hall effect (AHE) [3–16]. There are two main pathways for generating Weyl semimetals: breaking the inversion symmetry [17] or the time-reversal symmetry [18]. The first approach yielded the original discovery of nonmagnetic Weyl semimetals in the TaAs family [19–21]. The second approach recently led to the discovery of ferromagnetic Weyl semimetals (FM-WSMs) such as $Co_3Sn_2S_2$, Fe_3GeTe_2 and Co_2MnGa [22–25]. These FM-WSMs crystallize in a centrosymmetric lattice and exhibit collinear FM ordering. They have been intensely studied due to a giant AHE that resulted from the Berry curvature

around Weyl nodes, as confirmed by first-principles calculations [8,23–25].

In this article, we introduce CeAlSi as a FM-WSM that combines both routes mentioned above to generate Weyl nodes. CeAlSi crystallizes in the noncentrosymmetric space group $I4_1md$, a point we confirm via our second-harmonic-generation (SHG) experiments and first-principles calculations. The local f-moments of Ce^{3+} are found to interact within the noncentrosymmetric lattice and lead to a noncollinear FM order. The breaking of time-reversal symmetry in CeAlSi shifts the nodal positions and controls the magnitude of the AHE. We observe two different AHE responses in this material by orienting the magnetic field along the easy and hard magnetic axes. The lack of inversion symmetry, the in-plane noncollinear FM order, and the novel anisotropic AHE make CeAlSi a FM-WSM candidate that is distinct from other FM-WSMs.

II. MAIN RESULTS

Figure 1 summarizes our main results related to the discovery of a noncentrosymmetric FM-WSM with an anisotropic AHE. The body-centered tetragonal unit cell of CeAlSi

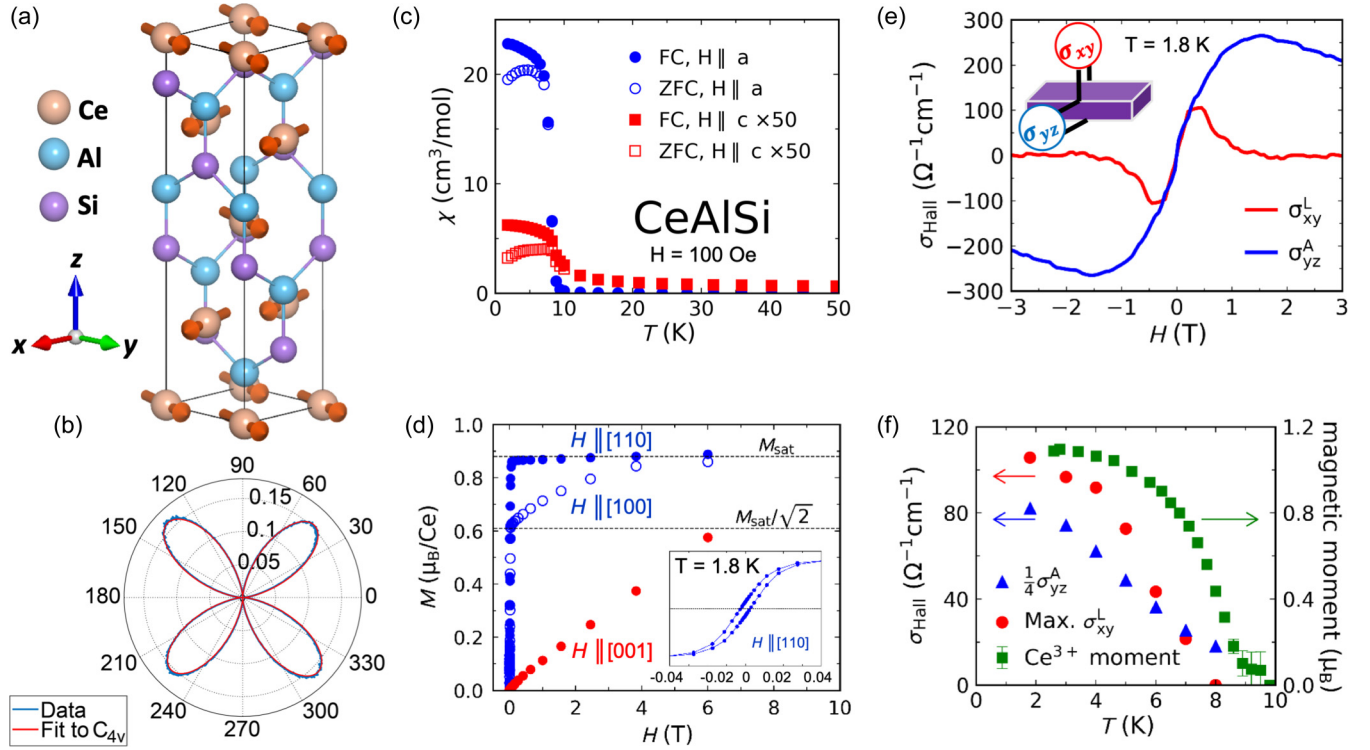*ar.bansil@northeastern.edu
†fazel.tafti@bc.edu

FIG. 1. Noncollinear order, noncentrosymmetric structure, and anomalous Hall effect in CeAlSi. (a) Noncollinear FM order in the tetragonal unit cell of CeAlSi. (b) Second-harmonic generation data refined in the noncentrosymmetric C_{4v} point group. (c) Anisotropic magnetic susceptibility as a function of temperature showing the in-plane easy-axis. (d) Magnetization curves with the field oriented along the [110], [100], and [001] directions. Inset shows hysteresis due to FM domains with a coercive field of 70 Oe. (e) Two distinct Hall responses are observed when a magnetic field is applied along the easy axis (σ_{yz}^A: anomalous Hall effect) or the hard axis (σ_{xy}^L: loop Hall effect). (f) Evolution of the magnetic order parameter (the Ce^{3+} moment), σ_{yz}^A, and σ_{xy}^L with temperature. Note that the order parameter here does not represent the saturated moment, which only drops by ~10% from 1.8 K to 8 K (see Sec. M3 in the Supplemental Material for details [26]).

[Fig. 1(a)] contains two vertical mirror planes (σ_v) but lacks a horizontal mirror plane (σ_h), thus breaking the inversion symmetry. The viability of an FM-WSM in such a structure (space group $I4_1md$) was first proposed by DFT calculations in CeAlGe [27,28]; however, experiments reported an antiferromagnetic (AF) order instead of an FM order [29–31]. On the contrary, our neutron diffraction and magnetization measurements show that CeAlSi hosts an FM order with net magnetization along the crystallographic [110] direction and an in-plane noncollinear spin texture as illustrated in Fig. 1(a). Although the noncollinear FM order distinguishes CeAlSi from other FM-WSMs, our neutron diffraction result shows that the angle between the noncollinear spins does not change with the applied magnetic field up to 8 T. Thus, the AHE observed in CeAlSi is distinct from the THE in noncoplanar magnets such as the MnGe and MnSi [4,5].

An important structural detail is the possibility of site mixing between Al and Si, which could invalidate the proposal of CeAlSi being a noncentrosymmetric FM-WSM. Intersite mixing can restore the σ_h mirror plane and change the space and point groups from noncentrosymmetric $I4_1md$ (C_{4v}) to centrosymmetric $I4_1/amd$ (C_{4h}). Neither x-ray nor neutron diffraction can reliably distinguish between the two space groups, see Sec. M1 in the Supplemental Material for details [26]. However, SHG can discriminate between these two structures because the SHG signal predominantly originates

from a bulk electric dipole in a noncentrosymmetric unit cell. Figure 1(b) shows a strong SHG signal ($\chi_{xxz} = 200$ pm/V) that is commensurate with the pronounced signal in GaAs [32] and fits the point group C_{4v}. Thus, we confirm the noncentrosymmetric space group $I4_1md$ as the correct structure, see Sec. M2 in the Supplemental Material for details [26].

CeAlSi is ferromagnetic with a strong magnetic anisotropy with an in-plane easy axis. As seen in Fig. 1(c), the in-plane magnetic susceptibility (blue) is 200 times larger than the out-of-plane susceptibility (red). The field dependence of magnetization [Fig. 1(d)] indicates that the [110] crystallographic direction as the easy axis (see Sec. M3 in the Supplemental Material for the persistent saturation of magnetic moments at high fields [26]). A gradual saturation of the $M(H\|[100])$ curve from $M_{sat}(H\|[110])/\sqrt{2}$ to $M_{sat}(H\|[110])$ implies the presence of zero-field magnetic domains with **M**$\|$ [110], [1 −10], [−110], and [−1 − 10] directions.

Due to the in-plane easy-axis orientation, we expect to observe an AHE when the magnetic field is oriented in the *ab*-plane. Figure 1(e) confirms such an anomalous Hall conductivity (the step in σ_{yz}^A), but it also reveals an unexpected signal (σ_{xy}^L), which is observed when the field lies along the hard axis. The superscript L in σ_{xy}^L stands for its loop-shaped behavior. Figure 1(f) shows the parallel temperature dependence of σ_{yz}^A, σ_{xy}^L, and the magnetic order parameter
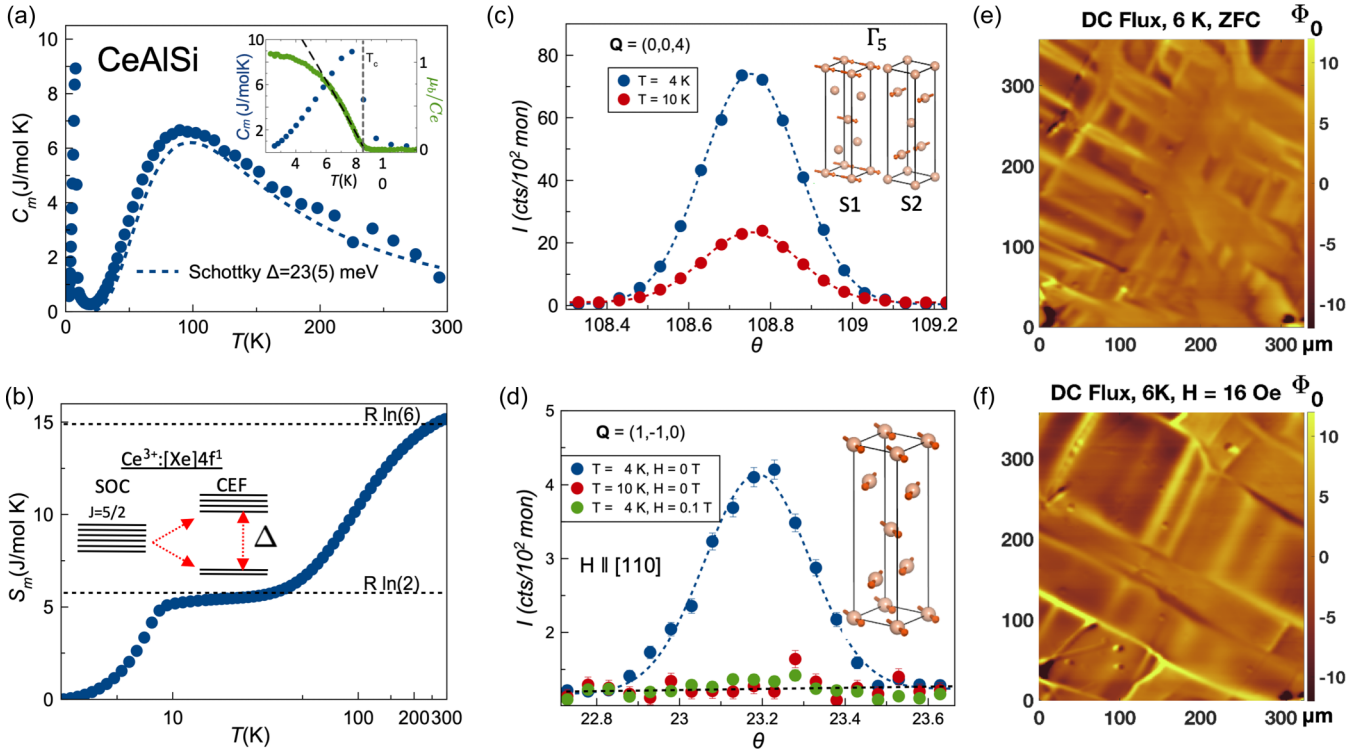
FIG. 2. Magnetic structure. (a) Magnetic specific heat as a function of temperature with a fit to the crystal electric field (CEF) levels. Inset shows a magnified view of the FM transition and a fit to the temperature dependence of the order parameter (magnetic moment per Ce atom). (b) Magnetic entropy as a function of temperature. Inset shows the CEF levels with a doublet ground state. (c) Neutron scattering Bragg peak at $\mathbf{Q} = (004)$. (d) Neutron scattering Bragg peak at $\mathbf{Q} = (1-10)$ is observed below $T_C = 8.2(3)$ K in zero field and suppressed by applying a field of 0.1 T along the [110] direction. (e) Scanning SQUID image of FM domains obtained at $T = 6$ K under zero field. (f) Large in-plane domains develop under a small in-plane field (16 Oe).

determined by neutron diffraction, suggesting that both Hall responses are controled by the FM order. We will examine these findings in detail in the remainder of this article.

III. IN-PLANE NONCOLLINEAR FM ORDER AND LARGE FM DOMAINS

The magnetic heat capacity (C_m) of CeAlSi in Fig. 2(a) exhibits a sharp FM transition at $T_C = 8.2(3)$ K and a broad (Schottky) peak at 80 K due to the crystal electric field (CEF) splitting of Ce^{3+} atomic levels. As shown in Fig. 2(b), the $J = 5/2$ sextet of Ce^{3+} splits into a doublet ground state and a quadruplet excited state, leading to two plateaus at $R \ln(2)$ and $R \ln(6)$ in the magnetic entropy S_m. From a fit to the C_m data in Fig. 2(a), we estimate a gap of $\Delta = 25$ meV between the doublet and the quadruplet, and identify the ground state of CeAlSi as a Kramers doublet with effective spin-1/2.

The in-plane noncollinear FM order of CeAlSi was determined by neutron diffraction. Figure 2(c) shows the $\mathbf{Q} = (004)$ peak corresponding to the FM ordering vector $\mathbf{k} = (000)$. The magnetic moment per Ce^{3+} (order parameter) is extracted from the intensity of this peak and plotted as a function of temperature in the inset of Fig. 2(a) along with the low-T heat capacity. These data are consistent with a second-order mean-field transition with the critical exponent $\beta = 0.48(4)$. Thus, the magnetic structure of CeAlSi belongs to a single irreducible representation (irrep) of the $I4_1md$

space group. The combination of our symmetry analysis (see Sec. M4 of Supplementary Material [26]) with the observation of several (00L) peaks allows us to conclude that CeAlSi orders in the Γ_5 manifold, where all spins lie in the ab-plane [Fig. 2(c)].

As illustrated in the inset of Fig. 2(c), the Γ_5 manifold allows for a complete decoupling of the Ce spins between the adjacent $(0,0,z+1/4)$ layers. We define $\mathbf{S_1}$ to be the Ce spin at $(0,0,0)$ and $\mathbf{S_2}$ to be that at $(0,1/2,1/4)$. Intensity of the neutron Bragg peaks with $\mathbf{k} = (000)$ and (110) ordering vectors is proportional to $\mathbf{S_1} + \mathbf{S_2}$ and $\mathbf{S_1}$-$\mathbf{S_2}$, respectively. Thus, the observation of both the ordering vectors in Figs. 2(c) and 2(d) suggests that both $\mathbf{S_1} + \mathbf{S_2}$ and $\mathbf{S_1}$-$\mathbf{S_2}$ are finite, so that the angle between $\mathbf{S_1}$ and $\mathbf{S_2}$, defined by $\theta = \cos^{-1}(\frac{\mathbf{S_1} \cdot \mathbf{S_2}}{\|\mathbf{S_1}\| \|\mathbf{S_2}\|})$, must be nonzero. Detailed refinement of the spin structure was then performed against 40 symmetrically distinct Bragg peaks collected at both 1.4 K and 10 K in zero-field, see Sec. M4 in Supplementary Material for details [26]. Assuming $\|\mathbf{S_1}\| = \|\mathbf{S_2}\|$, the refinement suggests a moment size of $1.2(2)\mu_B$ and $\theta = 70(30)°$, confirming the in-plane noncollinear FM order in CeAlSi [inset of Fig. 2(d)].

We performed scanning superconducting quantum interference device (SQUID) microscopy [33–35] to visualize the FM domain structure of CeAlSi. The images in Figs. 2(e) and 2(f) were obtained by scanning a SQUID sensor over the ab-surface of a polished crystal to measure the out-of-plane stray field from the in-plane domains. Although the domains
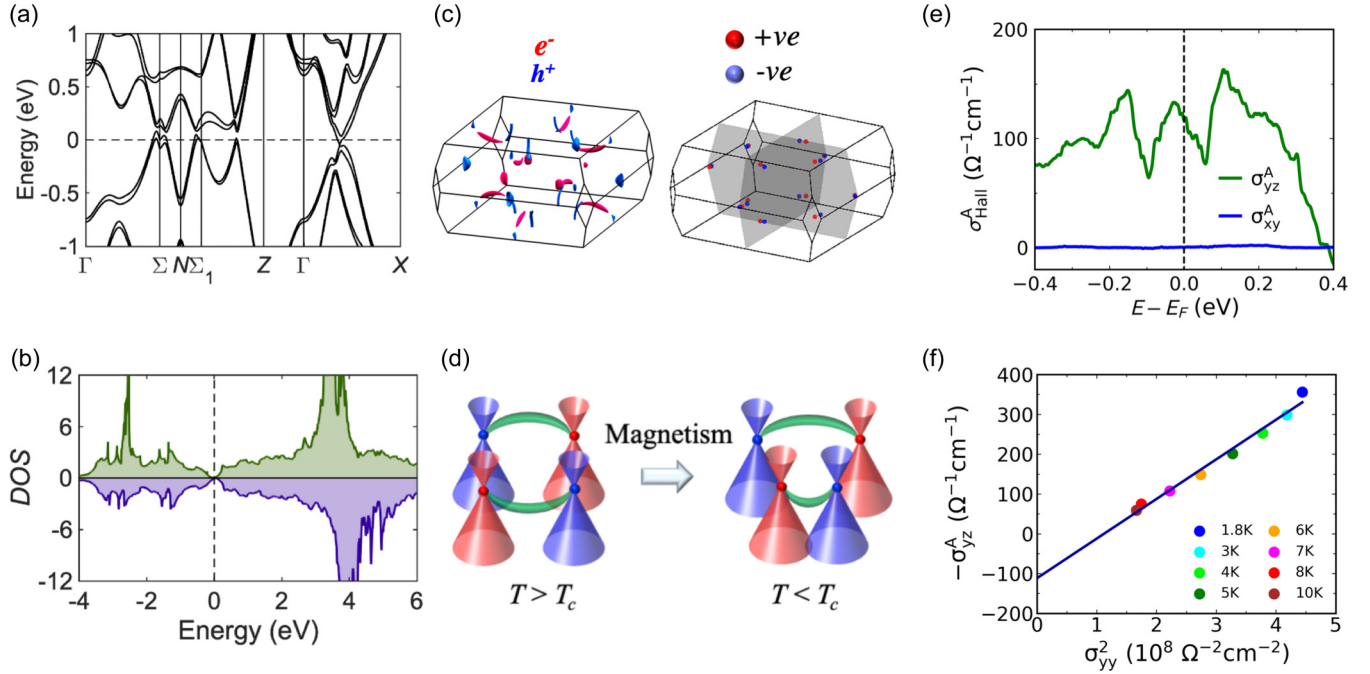
FIG. 3. Band structure and Weyl nodes. (a) Band structure of CeAlSi including spin-orbit coupling. (b) Partial density of states for the majority (green) and minority (purple) spin channels. (c) Electron (red) and hole (blue) pockets (left) and the Weyl nodes (right) are shown in the BZ. (d) Effects of breaking the inversion (left) and time-reversal (right) symmetries on the positions of Weyl nodes are shown schematically. (e) Theoretical values of the anomalous Hall conductivity with the field oriented in-plane (σ_{yz}^A) and out-of-the-plane (σ_{xy}^A). (f) Scaling behavior $\sigma_{yz}^A \propto \sigma_{yy}^2$ in CeAlSi, confirming an intrinsic AHE.

are small under zero-field-cooling [Fig. 2(e)], a weak in-plane field of a few Gauss is enough to generate large in-plane FM domains that are hundreds of microns across [Fig. 2(f)]. The development of large domains is also implied by the selection of a single domain revealed by neutron diffraction. Under a small in-plane field **H**∥ [110], the system selects a single domain with **M**∥ [110] among all symmetrically equivalent directions. As a result, the vector **S₁-S₂** only points along [1 −10] and the **Q** = (1–10) Bragg peak is suppressed accordingly, as seen in Fig. 1(d) when a field of 0.1 T is applied in the [110] direction. Magnitude of the observed DC flux is on the order of a few Φ_0, consistent with the remnant magnetization determined from the *c*-axis bulk magnetization measurements. According to our estimates based on the remanent *a*-axis magnetization, if the domains were to have flipped magnetization from the in-plane to the out-of-plane direction, it would have produced a DC signal on the order of hundreds of Φ_0, which is clearly not the case in Figs. 2(e) and 2(f), see Sec. M5 of Supplementary Material for details [26]). The picture that emerges from our neutron scattering and scanning SQUID measurements in CeAlSi is that of a noncollinear in-plane FM order with large domains.

IV. BAND STRUCTURE, SHIFTED WEYL NODES, AND INTRINSIC ANOMALOUS HALL CONDUCTIVITY

Band structure of CeAlSi [Fig. 3(a)] consists of small hole and electron pockets with a nearly vanishing density of states (DOS) at E_F [Fig. 3(b)]. The DOS in the majority and minority spin channels peaks at different energies [Fig. 3(b)]

and leads to FM ordering. The residual electron and hole pockets are illustrated in Fig. 3(c), which also shows the 12 pairs of Weyl nodes next to the $k_x = 0$ and $k_y = 0$ mirror-planes. We denote the four pairs of nodes located on the $k_z = 0$ plane as W_1, and the other eight as W_2. The W_1 nodes are 80–120 meV away from E_F but the W_2 nodes lie within 25 meV of the E_F, see Sec. M6 in the Supplementary Material for details [26]. All W_1 and W_2 Weyl fermions exhibit linear energy dispersions in all *k*-directions, suggesting that CeAlSi is a type-I WSM, see Sec. M6 and Fig. M6 of Supplementary Material for details [26]. This is different from the case of the related material CeAlGe that hosts both type-I and type-II Weyl nodes [27,28] driven by the stronger spin-orbit coupling of Ge and the slightly different Wyckoff site coordinates. Note that the Weyl nodes in CeAlSi result from a broken inversion symmetry ($\mathcal{I}$) and the effect of breaking the time-reversal symmetry ($\mathcal{T}$) at $T < T_C$ is to shift the positions of the Weyl nodes in the BZ [Fig. 3(d)] [9,27]. CeAlSi is thus a different FM-WSM, in sharp contrast to the centrosymmetric systems such as $Co_3Sn_2S_2$ [22,23], Fe_3GeTe_2 [24], and the Heusler alloys [36] where the Weyl nodes result from the broken $\mathcal{T}$.

We calculated the anomalous Hall conductivity (AHC) along the easy (σ_{yz}^A) and hard (σ_{xy}^A) axes as a function of the Fermi energy in Fig. 3(e) [8]. The magnitude of the theoretical AHC along the easy axis in Fig. 3(e) is comparable to the corresponding experimental values ($\sigma_{yz}^A = \rho_{zy}^A/\rho_{yy}^2$; $\rho_{zy}^A = \rho_{zy} - R_0 H$) [16,37] in Fig. 3(f). The scaling behavior between σ_{yz}^A and σ_{yy}^2 [Fig. 3(f)] indicates the presence of intrinsic and extrinsic contributions to the AHE [7], where the *y*-intercept codes the intrinsic contribution and the scaling with σ_{yy}^2
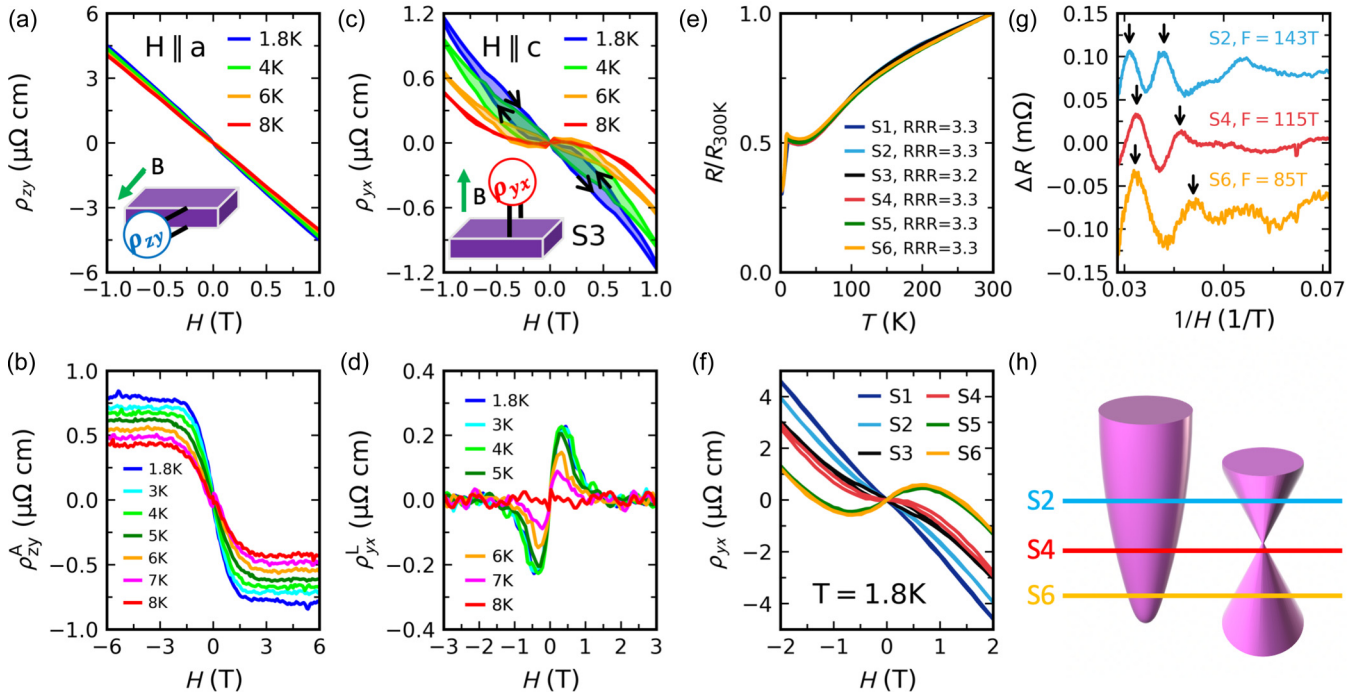
FIG. 4. Magnetic anisotropy and the loop Hall effect. (a) Hall resistivity ρ_{zy} measured at several temperatures with the field along the magnetic easy axis ($H \parallel a$). (b) Anomalous Hall resistivity ρ_{zy}^A derived from ρ_{zy}. (c) Hall resistivity ρ_{yx} measured at several temperatures with the field along the hard axis ($H \parallel c$). (d) Loop Hall resistivity ρ_{yx}^L derived from ρ_{yx}. (e) Normalized resistivity plotted as a function of temperature in samples S1-S6 with similar residual resistivity ratios. (f) Hall resistivity ρ_{yx} of samples S1-S6 measured at $T = 1.8$ K. (g) Quantum oscillations (QOs) in samples S2, S4, and S6, showing the evolution of the oscillation period. (h) Schematic band structure of CeAlSi illustrating an electron band, a Weyl crossing, and the Fermi levels of samples S2, S4, and S6. The decreasing QO frequency seen in panel (g) originates from the electron pocket (left) as the Fermi level shifts in samples S2, S4, and S6.

represents the extrinsic contribution [16,37]. Note that, according to the DFT, we do not expect an AHC ($\sigma_{xy}^A = 0$) along the magnetic hard-axis $H \parallel c$. Therefore, the observation of a loop-shaped Hall signal with $H \parallel c$ is a novel electromagnetic response as discussed further below.

V. ANISOTROPIC ANOMALOUS HALL EFFECT

CeAlSi displays two different anomalous Hall responses when measured under in-plane (easy-axis) and out-of-plane (hard-axis) magnetic fields; such a concurrence is quite unusual and has been reported only in a few cases [38]. We start by examining the Hall resistivity ρ_{zy} as a function of the in-plane field $H \parallel a$ [Fig. 4(a)]. We separate the conventional and anomalous Hall signals by fitting the data at $H > 1$ T to $\rho_{zy} = R_0 H + \rho_{zy}^A$. The conventional Hall effect ($R_0 H$) has a slope $R_0 = -3.9$ $\mu\Omega$cm T^{-1} corresponding to a small electron concentration $n_e = -1.6 \times 10^{20}$ cm^{-3} (0.0003 electrons per unit cell), consistent with the small value of DOS at the E_F in Fig. 3(b). The anomalous Hall resistivity ρ_{zy}^A is plotted as a function of field in Fig. 4(b). Note that ρ_{zy}^A does not exactly follow the magnetization [Fig. 1(d)] like other conventional AHE materials; this behavior has been observed in systems with noncollinear spin texture such as $Pr_2Ir_2O_7$ [39,40]. The anomalous Hall conductivity calculated from $\sigma_{yz}^A = \rho_{zy}^A/\rho_{yy}^2$ is plotted in Figs. 1(e) and 3(f). Magnitude of σ_{yz}^A is in agreement with the DFT results in Fig. 3(e).

Next, we discuss the Hall resistivity ρ_{yx} as a function of the out-of-plane field $H \parallel c$ (hard-axis) in Fig. 4(c), where an unusual loop is observed. This loop corresponds to different traces of $\rho_{yx}(H)$ between the field sweeps in the positive and negative directions [arrows in Fig. 4(c)]. It extends over a region of ± 2 T, two orders of magnitude larger than the magnetic coercive field [70 Oe, inset of Fig. 1(d)]. Notice that the loop-shaped Hall effect (LHE) does not scale with magnetization $M(H)$ and appears only when measured along the magnetic hard axis, unlike the AHE that saturates as the magnetization does and appears when the field is parallel to the easy axis. To study the temperature dependence of the LHE, we subtract the positive field sweep from the negative sweep and plot the loop Hall resistivity as $\rho_{yx}^L = \rho_{yx}(3 \rightarrow -3$ T$) - \rho_{yx}(-3 \rightarrow 3$ T$)$ at several temperatures [Fig. 4(d)]. The loop Hall conductivity σ_{xy}^L in Figs. 1(e) and 1(f) was calculated as $\sigma_{xy}^L = \rho_{yx}^L/\rho_{xx}^2$, see Sec. M7 in the Supplementary Material for details of the ρ_{xx} data [26].

To explore the link between the LHE and Weyl nodes, we measured samples with different separations between the Fermi level and the Weyl nodes. For this purpose, we selected six samples (S1-S6) with comparable residual resistivity ratios $RRR = R(300K)/R(2K)$ [Fig. 4(e)]. Slight off-stoichiometry of Si and Al in our samples (Sec. M8 of the Supplementary Material [26]) causes a shift of the Fermi level relative to the Weyl nodes [41]. Variations in the E_F between the samples is evident in Fig. 4(f), which shows three categories of Hall

curves: a linear ρ_{yx} with negative slope in samples S1 and S2; a moderately nonlinear ρ_{yx} with negative slope at all fields in S3 and S4; and a strongly nonlinear ρ_{yx} with positive slope at low fields and negative slope at high fields in S5 and S6. Since the slope of ρ_{yx} is related to the sign of charge carriers, we deduce that E_F crosses only electron pockets in samples S1 and S2, nearly crosses another hole pocket in S3 and S4, and crosses both the electron and hole pockets in S5 and S6 as illustrated in Fig. 4(h). The LHE is observed only in S3 and S4 where the E_F lies near the crossing of electron and hole bands, i.e. near the Weyl node [Fig. 4(h)].

To confirm the scenario of Fig. 4(h), we used Schubnikov–de Haas (SdH) oscillations to locate the E_F with respect to the Weyl nodes along the lines of prior work on Weyl and magnetic semimetals [42,43]. Figure 4(g) shows quantum oscillations for magnetic field between 15 and 33 T in samples S2, S4, and S6. The frequency of SdH oscillations, $F = A(\frac{\hbar}{2\pi e})$, is proportional to the extremal orbit area A, and it will change as we shift the E_F in the band structure. The E_F for each sample can then be pinned down by matching experimental and theoretical frequencies of the electron pocket [the left portion in Fig. 4(h)]. Through such an analysis, we obtain E_F values for samples S2, S4, and S6 to lie 32, 23, and 12 meV above the DFT-calculated value, respectively; see Sec. M9 of the Supplementary Material for details [26]. When we compare these E_F values to the energies of Weyl nodes, we find that all Weyl nodes lie away from the E_F in samples S2 and S6, but a set of W_2^2 Weyl nodes is located within 1 meV of the E_F in sample S4, as illustrated in Fig. 4(h); see also Tables M2 and M4 of the Supplementary Material [26]. Thus, we conclude that the LHE is observed only in samples where the E_F nearly crosses the Weyl nodes.

VI. OUTLOOK

In summary, CeAlSi is a unique noncentrosymmetric FM-WSM with an in-plane noncollinear FM order and novel anisotropic anomalous Hall responses along the easy and hard magnetic axes. In particular, CeAlSi exhibits the LHE which appears when the applied field lies along the hard axis. The LHE does not scale with either the field or the magnetization and is deeply connected with the Weyl nodes. The LHE is distinct from the THE [4–6] because the magnetic structure of CeAlSi may not support spin chirality or a skyrmion phase. To gain insight into the LHE in CeAlSi, we consider $Nd_2Ir_2O_7$, which also exhibits loop-shaped signals in magnetoresistance and Hall resistivity [44,45]. $Nd_2Ir_2O_7$ hosts an all-in-all-out magnetic order of null spin chirality and requires an explanation other than the THE for its loop responses. Recently, it was proposed that $Nd_2Ir_2O_7$, despite having an insulating ground state, is very close to a WSM phase and that slight doping or external pressure will turn it into a WSM [11,46,47]. As a result, topological Fermi arcs in $Nd_2Ir_2O_7$ projected from the Weyl nodes on the magnetic domain walls interact to form exotic surface states (SSs); these topological Fermi-arc-induced (FAI) SSs survive the annihilation of Weyl nodes in the insulating regime [48]. The FAI SSs were mapped out in $Nd_2Ir_2O_7$ by impedance spectroscopy [49], and can serve as special conducting channels responsible for the anomalous loop responses [44,45,48]. Keeping the preceding discussion

of the FAI SSs in mind, we compare and contrast $Nd_2Ir_2O_7$ and CeAlSi to gain insight into the origin of the LHE in CeAlSi as follows.

(1) $Nd_2Ir_2O_7$ is an overall AFM system with an all-in-all-out magnetic order, whereas CeAlSi hosts a noncollinear FM order. FAI SSs, however, only require the presence of the magnetic domain walls and the proximity of a WSM phase, and can thus be expected also in CeAlSi.

(2) Although $Nd_2Ir_2O_7$ is insulating whereas CeAlSi is semimetallic, FAI SSs can exist in both materials. In $Nd_2Ir_2O_7$, FAI SSs are remnant traces of the Fermi arcs in the system before it becomes insulating, while in CeAlSi, they are the Fermi arcs connecting the bulk Weyl nodes.

(3) The loop response in $Nd_2Ir_2O_7$ appears in both magnetoresistance (ρ_{xx}) and Hall resistivity ρ_{yx}, whereas in CeAlSi it only appears in ρ_{yx}. Generally, $\rho_{xx} \sim \sum_i^n \frac{\sigma_i}{1+\mu_i^2 B^2}$, where the summation extends over all conducting bands [50,51]. Since $\sigma_i = n_i e_i \mu_i$ is always positive, ρ_{xx} is dominated by the bands with large carrier densities n. Since $Nd_2Ir_2O_7$ is insulating, the FAI SSs provide the only conducting channels that dominate ρ_{xx}, and lead to the loop-shaped behavior. CeAlSi, in contrast, is metallic and its topological SSs fail to show a loop response in ρ_{xx} because the small density of states associated with these SSs is overwhelmed by the contribution from the bulk bands. On the other hand, note that $\rho_{yx} \sim \sum_i^n \frac{\sigma_i \mu_i}{1+\mu_i^2 B^2}$ and it can, therefore, be either positive or negative depending on the sign of the carriers in each band. In $Nd_2Ir_2O_7$, the FAI SSs being the only carriers, they also drive ρ_{yx} and yield a loop response. In CeAlSi, the electron and hole (bulk) contributions to ρ_{yx} nearly cancel [Fig. 3(c)] and, as a result, the topological SSs control the behavior of ρ_{yx} and drive its loop response in CeAlSi. This argument is consistent with our quantum oscillation results, which reveal an enhanced SS contribution (LHE) in the CeAlSi samples in which the Fermi energy lies close to the Weyl nodes.

CeAlSi will not only be amenable to ARPES studies due to its metallicity but it will also be suitable for device engineering and tuning of the Fermi arcs [52]. CeAlSi would thus provide an interesting material platform for exploring the physics of Weyl nodes and how these nodes are connected with the exotic electromagnetic responses of topological materials.

APPENDIX: METHODS

1. Crystal Growth

CeAlSi single crystals were grown by a self-flux method in both regular alumina crucibles and the Canfield crucible sets [53]. Both methods produced a similar crystal quality based on the PXRD, SHG, EDX, and resistivity measurements. In both methods, the starting materials were weighed in the ratio Ce:Al:Si = 1:10:1, placed inside a crucible in an evacuated quartz tube, heated to $1000°$ C at $3°$ C/min, stayed at $1000°$ C for 12 h, cooled to $700°$ C at $0.1°$ C/min, stayed at $700°$ C for 12 h, and centrifuged to decant the residual Al flux.

2. Band Structure

Density functional theory (DFT) calculations were performed using the experimental lattice parameters ($a = 4.252$ Å; $c = 14.5801$ Å) and the projector-augmented-wave (PAW) method implemented in the Vienna *ab initio* simulation package (VASP) [54]. The exchange-correlation effects were included using the generalized gradient approximation (GGA). The spin-orbit coupling (SOC) was included self-consistently [55,56]. An on-site Coulomb interaction was added for Ce f-electrons within the GGA + U scheme with $U_{\text{eff}} = 6$ eV. A Wannier tight-binding Hamiltonian was obtained from the *ab initio* results using the VASP2WANNIER90 interface, which was subsequently used in our topological properties calculations [57].

3. Transport, Heat Capacity, and Magnetization Measurements

Electrical resistivity was measured with the standard four-probe technique and the heat capacity was measured with the relaxation time method in a Quantum Design Physical Property Measurement System (PPMS) Dynacool. Magnetic heat capacity C_m was obtained by first measuring the heat capacity of nonmagnetic LaAlSi, and then subtracting it from the heat capacity of CeAlSi. DC magnetization experiments were conducted on the vibrating sample magnetometer in a Quantum Design MPMS3. The high-field experiments were performed using a 35 T DC Bitter magnet and a ^{3}He fridge with base temperature of 300 mK at the MagLab in Tallahassee. Comparison of the quantum oscillation frequencies between theory and experiment was carried out by using the DFT-generated bxsf file and the program SKEAF [58].

4. Neutron Diffraction

The nuclear structure of CeAlSi was characterized by a single-crystal time-of-flight experiment at 100 K on TOPAZ at the Oak Ridge National Lab. A three-dimensional (3D) diffraction map was acquired from 14 different sample positions allowing measurements of 6946 Bragg peaks where the nuclear structure factors were extracted following the method of Schultz *et al.* [59]. Structural refinements were performed using GSAS-II [60]. The magnetic structure was determined by diffraction experiments at the NIST Center for Neutron Research. The magnetic structure factors were determined using the thermal triple-axis spectrometer BT-7 by collecting rocking scans at various Bragg positions with incident and scattered neutron energies of 14.7 meV. Two single crystals were inserted in a top-loading CCR and a 7 T magnet to measure Bragg peaks in both the (H0L) and (HHL) planes. The order parameter measurement in Fig. 1(f) was performed with the SPINS spectrometer using 3.7 meV incident and scattered neutrons.

5. Second Harmonic Generation

The SHG data in Fig. 1(b) were taken at normal incidence on the [101] face of as-grown crystals for incoming(outgoing) wavelength of 1500(750) nm as a function of the incoming field polarization and measured for emitted light polarized parallel to the [010] crystalline axis [61]. In this geometry, all bulk contributions to the SHG signal from a $I4_1/amd$ space group are forbidden.

6. Scanning SQUID Imaging

We used scanning SQUID susceptometers with two gradiometric field coils and pickup loops [33]. The SQUID pickup loop and the field-coil average radii were 3.25 and 7 μm formed from Nb lines of 0.5 and 1 μm width, respectively. The scanning SQUID apparatus was housed in a closed-cycle Montana Instruments Fusion cryostat (Bozeman, Montana, USA) with the cryostat base temperature of 3 K.

[1] N. P. Armitage, E. J. Mele, and A. Vishwanath, Rev. Mod. Phys. **90**, 015001 (2018).

[2] A. Bansil, H. Lin, and T. Das, Rev. Mod. Phys. **88**, 021004 (2016).

[3] Y. Tokura, M. Kawasaki, and N. Nagaosa, Nat. Phys. **13**, 1056 (2017).

[4] A. Neubauer, C. Pfleiderer, B. Binz, A. Rosch, R. Ritz, P. G. Niklowitz, and P. Böni, Phys. Rev. Lett. **102**, 186602 (2009).

[5] N. Kanazawa, Y. Onose, T. Arima, D. Okuyama, K. Ohoyama, S. Wakimoto, K. Kakurai, S. Ishiwata, and Y. Tokura, Phys. Rev. Lett. **106**, 156603 (2011).

[6] J. Matsuno, N. Ogawa, K. Yasuda, F. Kagawa, W. Koshibae, N. Nagaosa, Y. Tokura, and M. Kawasaki, Sci. Adv. **2**, e1600304 (2016).

[7] N. Nagaosa, J. Sinova, S. Onoda, A. H. MacDonald, and N. P. Ong, Rev. Mod. Phys. **82**, 1539 (2010).

[8] Y. Yao, L. Kleinman, A. H. MacDonald, J. Sinova, T. Jungwirth, D.-S. Wang, E. Wang, and Q. Niu, Phys. Rev. Lett. **92**, 037204 (2004).

[9] K.-Y. Yang, Y.-M. Lu, and Y. Ran, Phys. Rev. B **84**, 075129 (2011).

[10] A. A. Burkov, Phys. Rev. Lett. **113**, 187202 (2014).

[11] K. Ueda, R. Kaneko, H. Ishizuka, J. Fujioka, N. Nagaosa, and Y. Tokura, Nat. Commun. **9**, 3032 (2018).

[12] S. Nakatsuji, N. Kiyohara, and T. Higo, Nature **527**, 212 (2015).

[13] A. K. Nayak, J. E. Fischer, Y. Sun, B. Yan, J. Karel, A. C. Komarek, C. Shekhar, N. Kumar, W. Schnelle, J. Kübler, C. Felser, and S. S. P. Parkin, Sci. Adv. **2**, e1501870 (2016).

[14] X. Li, C. Collignon, L. Xu, H. Zuo, A. Cavanna, U. Gennser, D. Mailly, B. Fauqué, L. Balents, Z. Zhu, and K. Behnia, Nat. Commun. **10**, 1 (2019).

[15] D. Destraz, L. Das, S. S. Tsirkin, Y. Xu, T. Neupert, J. Chang, A. Schilling, A. G. Grushin, J. Kohlbrecher, L. Keller, P. Puphal, E. Pomjakushina, and J. S. White, npj Quantum Mater. **5**, 5 (2020).

[16] H.-Y. Yang, B. Singh, B. Lu, C.-Y. Huang, F. Bahrami, W.-C. Chiu, D. Graf, S.-M. Huang, B. Wang, H. Lin, D. Torchinsky, A. Bansil, and F. Tafti, APL Mater. **8**, 011111 (2020).

[17] H. Weng, C. Fang, Z. Fang, B. A. Bernevig, and X. Dai, Phys. Rev. X **5**, 011029 (2015).

[18] X. Wan, A. M. Turner, A. Vishwanath, and S. Y. Savrasov, Phys. Rev. B **83**, 205101 (2011).

[19] S.-M. Huang, S.-Y. Xu, I. Belopolski, C.-C. Lee, G. Chang, B. Wang, N. Alidoust, G. Bian, M. Neupane, C. Zhang, S. Jia, A. Bansil, H. Lin, and M. Z. Hasan, Nat. Commun. **6**, 7373 (2015).

[20] B. Q. Lv, H. M. Weng, B. B. Fu, X. P. Wang, H. Miao, J. Ma, P. Richard, X. C. Huang, L. X. Zhao, G. F. Chen, Z. Fang, X. Dai, T. Qian, and H. Ding, Phys. Rev. X **5**, 031013 (2015).

[21] S.-Y. Xu, I. Belopolski, N. Alidoust, M. Neupane, G. Bian, C. Zhang, R. Sankar, G. Chang, Z. Yuan, C.-C. Lee, S.-M. Huang, H. Zheng, J. Ma, D. S. Sanchez, B. Wang, A. Bansil, F. Chou, P. P. Shibayev, H. Lin, S. Jia, and M. Z. Hasan, Science **349**, 613 (2015).

[22] Q. Wang, Y. Xu, R. Lou, Z. Liu, M. Li, Y. Huang, D. Shen, H. Weng, S. Wang, and H. Lei, Nat. Commun. **9**, 3681 (2018).

[23] E. Liu, Y. Sun, N. Kumar, L. Muechler, A. Sun, L. Jiao, S.-Y. Yang, D. Liu, A. Liang, Q. Xu, J. Kroder, V. Süß, H. Borrmann, C. Shekhar, Z. Wang, C. Xi, W. Wang, W. Schnelle, S. Wirth, Y. Chen, S. T. B. Goennenwein, and C. Felser, Nat. Phys. **14**, 1125 (2018).

[24] K. Kim, J. Seo, E. Lee, K.-T. Ko, B. S. Kim, B. G. Jang, J. M. Ok, J. Lee, Y. J. Jo, W. Kang, J. H. Shim, C. Kim, H. W. Yeom, B. I. Min, B.-J. Yang, and J. S. Kim, Nat. Mater. **17**, 794 (2018).

[25] I. Belopolski, K. Manna, D. S. Sanchez, G. Chang, B. Ernst, J. Yin, S. S. Zhang, T. Cochran, N. Shumiya, H. Zheng, B. Singh, G. Bian, D. Multer, M. Litskevich, X. Zhou, S.-M. Huang, B. Wang, T.-R. Chang, S.-Y. Xu, A. Bansil, C. Felser, H. Lin, and M. Z. Hasan, Science **365**, 1278 (2019).

[26] See Supplemental Material at http://link.aps.org/supplemental/10.1103/PhysRevB.103.115143 for details of structural analysis by x-ray and neutron diffraction, details of second harmonic generation, temperature dependence of M vs. H curves, symmetry analysis, and refinement of the canting angle by neutron scattering, details of SQUID imaging, detailed properties of Weyl points in CeAlSi, ρ_{xx} data for extracting AHC, details of EDX analysis, detailed quantum oscillation data, and the difference between ρ_{zy}^A and $R_S M$. The following references are not cited in the main text but in the Supplemental Material: A. S. Wills, Physica B: Condensed Matter **276-278**, 680 (2000); M. J. Cooper and R. Nathans, Acta Crystallogr. **23**, 357 (1967); R. K. Willardson and A. C. Beer, *Semiconductors and Semimetals*, Vol. 1 (Academic, New York, 1967); D. Shoenberg, *Magnetic Oscillations in Metals* (Cambridge University Press, Cambridge, England, 2009); M. Lee, Y. Onose, Y. Tokura, and N. P. Ong, Phys. Rev. B **75**, 172403 (2007).

[27] G. Chang, B. Singh, S.-Y. Xu, G. Bian, S.-M. Huang, C.-H. Hsu, I. Belopolski, N. Alidoust, D. S. Sanchez, H. Zheng, H. Lu, X. Zhang, Y. Bian, T.-R. Chang, H.-T. Jeng, A. Bansil, H. Hsu, S. Jia, T. Neupert, H. Lin, and M. Z. Hasan, Phys. Rev. B **97**, 041104(R) (2018).

[28] S.-Y. Xu, N. Alidoust, G. Chang, H. Lu, B. Singh, I. Belopolski, D. S. Sanchez, X. Zhang, G. Bian, H. Zheng, M.-A. Husanu, Y. Bian, S.-M. Huang, C.-H. Hsu, T.-R. Chang, H.-T. Jeng, A. Bansil, T. Neupert, V. N. Strocov, H. Lin, S. Jia, and M. Z. Hasan, Sci. Adv. **3**, e1603266 (2017).

[29] H. Hodovanets, C. J. Eckberg, P. Y. Zavalij, H. Kim, W.-C. Lin, M. Zic, D. J. Campbell, J. S. Higgins, and J. Paglione, Phys. Rev. B **98**, 245132 (2018).

[30] P. Puphal, V. Pomjakushin, N. Kanazawa, V. Ukleev, D. J. Gawryluk, J. Ma, M. Naamneh, N. C. Plumb, L. Keller, R. Cubitt, E. Pomjakushina, and J. S. White, Phys. Rev. Lett. **124**, 017202 (2020).

[31] T. Suzuki, L. Savary, J.-P. Liu, J. W. Lynn, L. Balents, and J. G. Checkelsky, Science **365**, 377 (2019).

[32] S. Bergfeld and W. Daum, Phys. Rev. Lett. **90**, 036801 (2003).

[33] I. Sochnikov, L. Maier, C. A. Watson, J. R. Kirtley, C. Gould, G. Tkachov, E. M. Hankiewicz, C. Brüne, H. Buhmann, L. W. Molenkamp, and K. A. Moler, Phys. Rev. Lett. **114**, 066801 (2015).

[34] I. Sochnikov, A. J. Bestwick, J. R. Williams, T. M. Lippman, I. R. Fisher, D. Goldhaber-Gordon, J. R. Kirtley, and K. A. Moler, Nano Lett. **13**, 3086 (2013).

[35] B. W. Gardner, J. C. Wynn, P. G. Björnsson, E. W. J. Straver, K. A. Moler, J. R. Kirtley, and M. B. Ketchen, Rev. Sci. Instrum. **72**, 2361 (2001).

[36] Z. Wang, M. G. Vergniory, S. Kushwaha, M. Hirschberger, E. V. Chulkov, A. Ernst, N. P. Ong, R. J. Cava, and B. A. Bernevig, Phys. Rev. Lett. **117**, 236401 (2016).

[37] Y. Tian, L. Ye, and X. Jin, Phys. Rev. Lett. **103**, 087206 (2009).

[38] K. S. Takahashi, H. Ishizuka, T. Murata, Q. Y. Wang, Y. Tokura, N. Nagaosa, and M. Kawasaki, Sci. Adv. **4**, eaar7880 (2018).

[39] Y. Machida, S. Nakatsuji, Y. Maeno, T. Tayama, T. Sakakibara, and S. Onoda, Phys. Rev. Lett. **98**, 057203 (2007).

[40] L. Balicas, S. Nakatsuji, Y. Machida, and S. Onoda, Phys. Rev. Lett. **106**, 217204 (2011).

[41] C. Y. Guo, F. Wu, Z. Z. Wu, M. Smidman, C. Cao, A. Bostwick, C. Jozwiak, E. Rotenberg, Y. Liu, F. Steglich, and H. Q. Yuan, Nat. Commun. **9**, 4622 (2018).

[42] R. Schönemann, N. Aryal, Q. Zhou, Y.-C. Chiu, K.-W. Chen, T. J. Martin, G. T. McCandless, J. Y. Chan, E. Manousakis, and L. Balicas, Phys. Rev. B **96**, 121108(R) (2017).

[43] H.-Y. Yang, J. Gaudet, A. A. Aczel, D. E. Graf, P. Blaha, B. D. Gaulin, and F. Tafti, Phys. Rev. B **98**, 045136 (2018).

[44] K. Ueda, J. Fujioka, Y. Takahashi, T. Suzuki, S. Ishiwata, Y. Taguchi, M. Kawasaki, and Y. Tokura, Phys. Rev. B **89**, 075127 (2014).

[45] S. M. Disseler, S. R. Giblin, C. Dhital, K. C. Lukas, S. D. Wilson, and M. J. Graf, Phys. Rev. B **87**, 060403(R) (2013).

[46] W. Witczak-Krempa and Y. B. Kim, Phys. Rev. B **85**, 045124 (2012).

[47] K. Ueda, J. Fujioka, Y. Takahashi, T. Suzuki, S. Ishiwata, Y. Taguchi, and Y. Tokura, Phys. Rev. Lett. **109**, 136402 (2012).

[48] Y. Yamaji and M. Imada, Phys. Rev. X **4**, 021035 (2014).

[49] E. Y. Ma, Y.-T. Cui, K. Ueda, S. Tang, K. Chen, N. Tamura, P. M. Wu, J. Fujioka, Y. Tokura, and Z.-X. Shen, Science **350**, 538 (2015).

[50] H.-Y. Yang, T. Nummy, H. Li, S. Jaszewski, M. Abramchuk, D. S. Dessau, and F. Tafti, Phys. Rev. B **96**, 235128 (2017).

[51] J. M. Ziman, *Principles of the Theory of Solids* (Cambridge University Press, Cambridge, England, 1972).

[52] R. Ilan, A. G. Grushin, and D. I. Pikulin, Nat. Rev. Phys. **2**, 29 (2020).

[53] P. C. Canfield, T. Kong, U. S. Kaluarachchi, and N. H. Jo, Philos. Mag. **96**, 84 (2016).

[54] G. Kresse and J. Furthmüller, Phys. Rev. B **54**, 11169 (1996).

[55] G. Kresse and D. Joubert, Phys. Rev. B **59**, 1758 (1999).

[56] J. P. Perdew, K. Burke, and M. Ernzerhof, Phys. Rev. Lett. **77**, 3865 (1996).

[57] N. Marzari and D. Vanderbilt, Phys. Rev. B **56**, 12847 (1997).

[58] P. M. Rourke and S. R. Julian, Comput. Phys. Commun. **183**, 324 (2012).

[59] A. J. Schultz, M. R. V. Jørgensen, X. Wang, R. L. Mikkelson, D. J. Mikkelson, V. E. Lynch, P. F. Peterson, M. L. Green, and C. M. Hoffmann, J. Appl. Crystallogr. **47**, 915 (2014).

[60] B. H. Toby and R. B. Von Dreele, J. Appl. Crystallogr. **46**, 544 (2013).

[61] B. Lu, J. D. Tran, and D. H. Torchinsky, Rev. Sci. Instrum. **90**, 053102 (2019).